Titre: Title:	Failure mechanisms of coiling fibers with sacrificial bonds made by instability-assisted fused deposition modeling
Auteurs: Authors:	Shibo Zou, Daniel Therriault, & Frederick Gosselin
Date:	2018
Type:	Article de revue / Article
Référence: Citation:	Zou, S., Therriault, D., & Gosselin, F. (2018). Failure mechanisms of coiling fibers with sacrificial bonds made by instability-assisted fused deposition modeling. Soft Matter, 14(48), 9777-9785. https://doi.org/10.1039/c8sm01589a

Document en libre accès dans PolyPublie
Open Access document in PolyPublie

URL de PolyPublie: PolyPublie URL:	https://publications.polymtl.ca/10420/
Version:	Version finale avant publication / Accepted version Révisé par les pairs / Refereed
Conditions d'utilisation: Terms of Use:	Tous droits réservés / All rights reserved

Document publié chez l'éditeur officiel
Document issued by the official publisher

Titre de la revue: Journal Title:	Soft Matter (vol. 14, no. 48)
Maison d'édition: Publisher:	Royal Society of Chemistry
URL officiel: Official URL:	https://doi.org/10.1039/c8sm01589a
Mention légale: Legal notice:	©2018. This is the author's version of an article that appeared in Soft Matter (vol. 14, no. 48) . The final published version is available at https://doi.org/10.1039/c8sm01589a

Failure mechanisms of coiling fibers with sacrificial bonds made by instability-assisted fused deposition modeling

Shibo Zou, Daniel Therriault, Frédérick P. Gosselin*

Laboratory for Multiscale Mechanics (LM2), Department of Mechanical Engineering, École Polytechnique de Montréal, Montréal, Canada

Corresponding author, frederick.gosselin@polymtl.ca

Abstract: Instability-assisted 3D printing is a method for producing microstructured fibers with sacrificial bonds and hidden lengths which mimic nature's toughening mechanisms found in spider silk. This hierarchical structure increases the effective toughness of poly(lactic acid) (PLA) fibers by 240% − 340% in some specimens. Nevertheless, many specimens show worse toughness as low as 25% of that of the benchmark straight fiber due to the incomplete release of hidden lengths caused by premature failures. Here, we report mechanical tests and simulations of microstructured fibers with coiling loops that identify the material plastic deformation as being crucial to fully release the hidden lengths. Without sufficient material yielding, high local tensile stress results from the bending-torsion-tension coupled deformation of the coiling loop and induces crack initiation at the fiber backbone during the loop unfolding process. On the other hand, the influence of bond-breaking defect is found to be negligible here. Moreover, for a number of broken bonds beyond a critical value, the accumulated elastic energy along the released loops induces a high strain rate (~ 1500 mm/mm/s) in quasi-static tensile test, which fractures the fiber backbone within 0.1 ms after the breaking of a new bond. We also show a size effect in fused deposition modeling (FDM) extruded PLA fibers, which results in higher effective toughness (~ 5 times the performance of the straight fiber benchmark) in small coiling fibers (dia. = 0.37 mm), due to the better ductility in bending and torsion than large fibers (dia. = 1.20 mm). The failure mechanisms of single microstructured fiber presented here lay the groundwork for further optimizations of fiber arrays in the next generation of high energy-absorption composites for impact protection and safety-critical applications.

Introduction

Spider silk outperforms most synthetic materials in terms of specific toughness [1]. This toughness has been attributed to the unique protein structure in spider silk: stiff nanocrystals embedded in a less orderly semi-amorphous matrix which is rich in hydrogen bonding [2]. Upon stretching, these weak hydrogen bonds act as sacrificial bonds [3] whose early breakage releases the entangled protein chains in the semi-amorphous domain. The breaking of hydrogen bonds and the unravelling of hidden protein chains contribute to the high extensibility and toughness of spider silk. Similar toughening mechanisms are also found in bone [4], nacre [5] and mussel byssus threads [6].

Recently, the concept of sacrificial bonds and hidden length for toughness enhancement has inspired several experimental [7-10] and numerical [11] studies of structured fibers at the microscale. This hierarchical structure consisting of sacrificial bonds and hidden length is successfully implemented by introducing slip knots [7-9] or weak self-adhesions [10, 11] into natural or synthetic fibers. However, premature failures which cause incomplete release of fiber hidden length are also found in these studies, resulting in an occasional overall toughness decrease. Pugno et al. [8] found that a too tight overhand loop knot in silk fiber can lead to early fiber failure at the knot entrance, leaving the hidden length unreleased. They further optimized the knot configuration and achieved the full release of the fiber hidden length, resulting in 300% − 400% toughness enhancement in silk fibers [8] and up to 3000% in carbon nanotube microfibers

[9] with one single noose knot. Passieux et al. [10] introduced weakly fused bonds as sacrificial bonds into poly(lactic acid) (PLA) fibers with coiling or alternating loops by instability-assisted 3D printing. They found that the fiber backbone sometimes fails early before all hidden lengths are released. These premature failures result in the large scatter in the toughness values of microstructured fibers. The toughness of the microstructured fiber is sometimes as low as 25% of that of the straight fiber. They attributed these premature failures to the cusp formed during the loop unfolding process and the surface defect left by bond breaking. Koebley et al. [11] found similar hierarchical structure with coiling loops in loxosceles silk. They supposed that the cusp and bond-breaking defect can be avoided by the slender ribbon structure and silk-to-silk adhesion in loxosceles silk, instead of the cylindrical fiber structure and physically fused bond in Passieux et al.'s work. However, premature failures are still found in loxosceles silk to inhibit the hidden length from being fully released, resulting in the structured fibers' overall toughness being only 27% − 64% of the straight fibers. Koebley et al. [11] attributes these premature failures to material imperfections and incorrect test conditions. Nevertheless, the mechanics behind these premature failures in microstructured fibers with sacrificial bonds is still unclear.

In this article, we use the instability-assisted fused deposition modeling (IFDM) technique developed by Passieux et al. [10] to fabricate microstructured fibers with sacrificial bonds. As shown in Figure 1a, the molten PLA filament is deposited in ambient condition onto a moving belt. The filament swings and coils on itself due to a similar instability as found in the "elastic [12] / fluid mechanical [13] / molten glass [14] sewing machine". After the polymer is solidified in ambient air, weakly fused bonds are formed at the intersections along the fiber (Figure 1a). As described by Passieux et al. [10], these bonds, i.e., bonds α and β in Figure 1b, act as sacrificial bonds in uniaxial tensile test. They are supposed to break one by one, leading to a saw-tooth tensile curve as shown in Figure 1c. The area under the tensile curve represents the energy absorption contributed by the breaking of bonds and the unfolding of corresponding loops. The premature failure, in which the fiber backbone fractures before bond α breaks, reduces fiber strength and toughness. Passieux et al. [10] found that the failure modes are different with respect to fracture time and location due to the interrelation between the varying slenderness with fiber patterns and the number and strength of sacrificial bonds. Among their specimens, those with a coiling pattern exhibit varieties of failure modes and the lowest toughness value. Therefore, we purposely select these underperforming coiling pattern fibers to understand their failure. We do so by fixing the ratio of the filament extruding speed V_E to the belt moving speed V_B (Figure 1a). The relative strength of the bonds to the fiber backbone is kept constant in two coiling fibers at different scales (large fiber: $d = 1.20$ mm; small fiber: $d = 0.37$ mm) by fixing the ratio of the deposition height H to the fiber diameter d (Figure 1a). We systematically categorized the failure modes of coiling fibers by testing specimens with varying number of sacrificial bonds. Complementing this experimental study, we performed nonlinear finite element analysis (FEA) in order to find the root cause for each failure mode.

Results and discussion

According to the differences in fracture time and location among coiling fiber specimens in uniaxial tensile test, we categorize five failure modes: axial, bending, torsional, bond and dynamic failure. In axial failure, the coiling loop is unfolded and fully straightened until the fiber breaks in the middle of the loop (Figure 2a [i]). Apparent necking is observed at both fracture ends (Figure 2a [ii]). The fracture surface shows extended polymer tongues which indicates a large amount of plastic deformation (Figure 2a [iii]). In bending failure, the fiber also breaks in the middle of the loop (Figure 2b [i]). Compared to axial failure, the crack in bending failure initiates much earlier from the cusp at the top of the loop. Typical butterfly pattern can be seen on the fracture surface with stress whitening at the two sides (Figure 2b [ii]). Similar extended polymer tongues as in the axial failure are also found at the bottom half of the fracture surface (Figure 2b [iii]).

In torsional and bond failure, the fiber does not break in the middle of the loop but near it (Figure 2c [i] & 2d [i]). In torsional failure, the fracture shows a spiral pattern (Figure 2c [ii]) which indicates that the fiber breaks due to the maximum tensile stress under torsion. Smooth crack initiation region with crazing and rough crack propagation region with hackles can be seen on the fracture surface (Figure 2c [iii]), which indicate the brittle nature of the fracture [15]. In bond failure, a similar spiral fracture pattern is observed (Figure 2d [ii]). The fracture plane is found right across the surface defect left by the bond breaking, which would suggest that the defect might have played a bigger role in this fracture. However, the scanning electron microscopy (SEM) image shows that the crack initiates not from the defect, but from a pigment aggregate inside the fiber (Figure 2d [iii]). This indicates that in this case, the fracture is more likely caused by a combination of the flaw and the maximum tensile stress, but not the bond-breaking defect.

The dynamic failure is different from all the above failure modes in terms of the fracture timescale after the breaking of sacrificial bond. In the above failure cases, the fracture of the fiber backbone happens at least 930 ms after the breaking of a sacrificial bond during the unfolding process. While in dynamic failure, the fiber backbone breaks within only 0.099 ms after the breaking of a sacrificial bond (Figure 2e [i]). The fiber breaks at a similar location as in bending failure, but has a more brittle appearance. No material distortion is observed near the fracture surface and the two fracture pieces fit with each other perfectly (Figure 2e [ii]). On the fracture surface, the smooth crack initiation region suddenly translates to the rough crack propagation region (Figure 2e [iii]), which indicates a sharp increase of stress and crack propagation speed [16].

In order to understand the failure mechanisms of the coiling fiber, we performed quasi-static FEA of two coiling loops under uniaxial tension. First, to explore the effect of material characteristics on structure behavior, we compared the bond breaking process of the coiling fiber with two different material models: linear elasticity and multilinear plasticity (Figure 3). In order to compensate the difference in gauge length between tensile test and simulation, we define an apparent strain as $\varepsilon^* = \Delta l / l_0 \times 100\%$, where Δl is the axial displacement and l_0 is the initial length of the coiling fiber between the grips. Before the first bond (bond β in Figure 3) breaks, the coiling fiber is stiff as the hidden lengths is bypassed by the load path. Both the elastic and plastic FEA overestimate the stiffness of the overall structure (Figure 3 inset). This is probably due to the fiber slippage in the grips during the tensile test, or the imperfect modeling of sacrificial bond via rigid surface constraint in the simulation. After bond β breaks, the pulling force drops due to the release of hidden length (loop β). Then the force increases as loop β is unfolded and straightened. The elastic FEA overestimates the pulling force and thus predicts the breaking of the next bond (bond α) significantly earlier than the plastic FEA. After bond α breaks, the two loops in the elastic FEA share the same amount of deformation (Figure 3, contour plot at $\varepsilon^* = 102\%$ in the elastic FEA) due to the recovery of elastic strain along loop β. Under further stretching, the two loops behave similarly to a coiled elastic spring [17, 18] due to the absence of plastic deformation in the elastic FEA. However, in the tensile test, loop α and β display unequal amount of deformation after the breaking of bond α (Figure 3, at $\varepsilon^* = 148\%$). This indicates a large amount of plastic deformation along loop β, which cannot be recovered after the breaking of sacrificial bond α. The plastic FEA's prediction of the deformation of the two loops after the breaking of bond α is much closer to the experimental result. The two loops behave very differently from the coiled elastic spring [17, 18] due to the plastic strain accumulated along the loops each time after the bond breaks. Even though some loops, like the loop β in Figure 3, experience cyclic loading, fatigue [19] is not considered here, because the fiber breaks within the last unfolded loop in 157 out of 160 failure cases observed in this work.

The plastic FEA is in quantitative and qualitative agreement with the tensile test in respect of the bond breaking, the reaction force and unfolding geometry of the coiling loop (Figure 3). We hence calculate

local curvature, as well as shear and axial strains (calculation details are illustrated in Figure S1) along the fiber to further analyze the variation of fracture time and location in test specimens. In order to simplify the analysis, we define an unfolding percentage of the hidden length in each coiling loop as $p = 100 \times s / l_h$, where s is the axial displacement after the breaking of corresponding sacrificial bond and l_h is the hidden length. The hidden length of each coiling loop is considered constant in all test specimens. In Figure 4a, the fibers' fracture force and unfolding percentage at break for all failure modes are superimposed on a schematic representation of the force-displacement curve of one coiling loop from axial failure specimen. In Figure 4b - d, the fracture location along the coiling loop and unfolding percentage at break are plotted for each failure mode against local curvature, shear and axial strains along the second releasing loop α in Figure 3. This superimposition of statistical test data of failure modes on simulation results enables us to analyze the influence of different deformation components on each failure mode. Since the large fiber provides more comprehensive experimental data on each failure mode than the small fiber, only simulation and test results of the large fiber are presented in Figure 4. Due to the geometric similarity, the small fiber is expected to have the same local strain as the large fiber at equivalent location along the fiber in the static simulation.

After the breaking of a sacrificial bond, the pulling force rises rapidly mainly due to the increase of curvature in the middle of the loop. As the unfolding process proceeds, although the curvature continues to increase (Figure 4b), the pulling force reaches a short plateau after p exceeds 20% (Figure 4a). From the FEA contour plots with equivalent unfolding percentage (at $\varepsilon^* = 148\%$) in Figure 3, it can be seen that the middle of the loop has reached the tensile strength of the material (70.5 MPa, Figure S2). Material yielding in the middle of the loop slows down the rate of increase of the pulling force. At this stage, the bending-dominated deformation of the coiling loop leads to high tensile stresses. This induces crack initiation at the top of the middle loop (Figure 2b, at $t = 930$ms), giving rise to a sudden drop on the pulling force curve (Figure 4a, △ and blue dashed lines). As the crack propagates, the remaining material in the middle of the loop continues to carry the load. Further stretching straightens the two broken loop pieces, causing the force to increase even after the crack initiation. In the end, the final fracture of the fiber in bending failure (Figure 4a, ▲) happens at $p = 70\% - 95\%$ with a relatively lower fracture force compared to the representative pulling force curve.

After p exceeds 50%, shear strain increases rapidly in the middle of the loop (Figure 4c). However, the fiber in torsional failure (Figure 4c, ●) never breaks in the middle of the loop. Large material distortion is observed in the middle of the loop in SEM images of the torsional failure specimen (Figure 5a). This indicates a large amount of plastic deformation which may prevent the crack initiation as in bending failure. The fiber in torsional failure can break at either sides of the loop around 5 to 8 mm away from the middle (Figure 4c, ● , $L_a = 4$ to 7 mm and 17 to 20 mm). The fiber in bond failure breaks at similar unfolding percentages (Figure 4c, ■ , $p = 60\% - 100\%$), with the fracture location restricted around the bond-breaking defect. In order to understand the fracture in torsional and bond failure (Figure 5b, c), the distribution of the first principal stress across the fiber section is given at selected locations along the fiber at $p = 80\%$ in Figure 5d. As L_a increases from 15.63 mm to 23.63 mm, the first principal stress reaches the maximum 70.5 MPa near the top surface of the fiber. It can be seen that this maximum stress region across the fiber section is relatively larger at $L_a = 17$ to 21 mm than other places along the fiber. This corresponds well with the distribution of the fracture locations along the fiber in torsional failure (Figure 5d, ●) and bond failure (Figure 5d, ■). Also, the location of the maximum stress region within the fiber cross section (Figure 5d, at $L_a = 18.05$, 19.27 and 20.47 mm) perfectly matches with the crack initiation region in SEM images of the torsional failure (Figure 5b [ii]) and bond failure specimen (Figure 5c [ii]). This indicates that the fiber fails due to the maximum tensile stress in torsional and bond failure. This also reinforces our previous speculation about the insignificance of bond-breaking defect

in bond failure based on fractographic analysis. Therefore, if the fiber avoids the bending crack by sufficient material yielding in the middle of the loop, further stretching results in two growing maximum tensile stress regions along the fiber at $L_a = 3$ to 7 mm and 17 to 21 mm. These tensile stress regions are generated by the combination of bending, torsion and axial tension. The crack in torsional and bond failure initiates from the largest maximum stress region, then propagates through a spiral pattern due to the torsional strain along the fiber. This explains the spiral fracture morphology in torsional and bond failure. Since the size of the maximum stress region is similar from $L_a = 3$ to 7 mm and 17 to 21 mm along the fiber, the crack always initiates at the weakest point. This is sometimes contributed by a flaw, such as a color pigment shown in Figure 5c [ii]. This maximum stress region leads to the large variation of fracture location in torsional and bond failure. The hidden length is fully released when p reaches 100%. The pulling force increases rapidly due to the tensioning of the fiber backbone. The final axial failure (Figure 4d, ✻) happens in the middle of the loop, where the maximum axial strain locates.

The probabilities of different failure modes are also found to be related to the size of the fiber (Figure 6a, b) and the number of sacrificial bonds n_t in test fibers (Figure 6b - d). In large fibers, axial failure happens only when there is one bond in the test fiber (Figure 6c). As n_t increases, the proportion of bending failure decreases, probably due to the less strict lateral constraints associated with the existence of more loops. The average number of actually broken bonds n_b stays around two (Figure 6b, black solid line). However, different results are observed in a geometrically similar coiling fiber with a smaller diameter (0.37 mm, Figure 6a in red). All test bonds can be broken when $n_t \leq 3$ (Figure 6b, red dashed line). The fracture surface of axial failure (Figure 6e [i]) shows very similar necking characteristics to those of the large fiber (Figure 2a [iii]). Bending, torsional and bond failures are almost absent in the small fiber, except for one bending failure case at $n_t = 4$ (Figure 6d), which is probably caused by the pigment aggregate in the crack initiation region on the fracture surface (Figure 6e [ii]). In order to investigate the difference of the failure behavior between the large and small fibers, bending failure at $n_t = 2$ in the large fiber is chosen to compare with the small fiber in Figure 6f. The two fibers show very similar apparent stress-strain curves and bond strengths, which is attributed to the same V_E / V_B and H / d ratios kept in their fabrication. Due to the geometric similarity, we have $\kappa_L / \kappa_S = d_S / d_L$, where κ is the fiber curvature; d is the fiber diameter; the indices L and S stand for the large and small fiber, respectively. Therefore, the maximum bending stress at the top of the loop $\sigma = E\kappa d / 2$ is the same for the large and small fibers, assuming a constant Young's modulus E in both fibers. However, the crack initiates in the large fiber, but not in the small fiber (Figure 6f). This indicates a size effect concerning the fiber's ductility, despite the fact that in uniaxial tensile tests, large and small straight fibers exhibit identical behavior (Figure S3).

In order to further understand this size effect, we performed three-point bending tests on the large and small straight fibers under the strain rate (0.33 mm/mm/s, Figure S4a) which corresponds to what the middle of the loop experiences during the unfolding process. Whereas the large and small straight fibers behave identically in tensile test (Figure S3), they differ in ductility in three-point bending test (Figure 6g). Six out of ten large fiber specimens show bending cracks at the bottom of the fiber around the engineering strain of 0.2, while all ten small fiber specimens survive until the engineering strain of 0.35 without any visible cracks. The small difference in crystallinity (large fiber: 2.5%; small fiber: 1.1%. Figure S5) might account for this size effect. Compared with the large fiber, the relatively faster cooling rate in the small fiber after extrusion leads to two times lower crystallinity and thus more amorphous structure with higher ductility. Another possible explanation for this size effect is the strain gradient plasticity theory [20]. In tension, the fiber has a uniform strain distribution within the cross sectional area, while in bending and torsion, the strain is maximum at the surface but zero along the neutral axis, resulting in a strain gradient. The strain gradient enhances material hardening, which has been also

observed in polymers such as epoxy and polycarbonate [21]. Hence, the greater strain gradient makes the small fiber more ductile than the large fiber in the three-point bending test. We are led to believe that the higher ductility prevents bending, torsional and bond failures in the small fiber, resulting in more broken bonds than that in the large fiber.

After $n_t \geq 5$, the small fibers always fail in dynamic failure with n_b around 4 (Figure 6b, d). This indicates that dynamic failure is somehow related to the number of already broken bonds in the test fiber. Recollecting from Figure 2e [i], in dynamic failure, the newly releasing loop is suddenly retracted due to the springback of previously unfolded loops after the breaking of a sacrificial bond. According to the simulation, this springback is also related to the material's characteristic, as the loop retraction after the breaking of a sacrificial bond in the elastic FEA is much larger than that in the plastic FEA. Therefore, we think that dynamic failure is triggered once the accumulated elastic energy along previously unfolded loops reaches a critical value. The inducing retraction causes a local strain rate as high as 1492 mm/mm/s (Figure S4d) on the top surface in the middle of the newly releasing loop, which fractures the fiber backbone immediately. That is the reason why both the fracture surfaces of the small (Figure 6e [iii]) and large (Figure 2e [iii]) fibers in dynamic failure show a sharp transition from the smooth crack initiation region to the rough crack propagation region.

Conclusions

Simulation and experiment both indicate that material yielding is indispensable to fully release the hidden length of the coiling fiber. If material yielding is insufficient along the fiber throughout the loop unfolding process, the fiber backbone will fracture at or besides the middle of the loop due to high local tensile stress, resulting in bending, torsional or bond failures. After the breaking of a certain number of bonds, the accumulated elastic energy along the already unfolded loops will induce a high strain rate recoil that fractures the fiber backbone immediately in the middle of the loop. The influence of bond-breaking defect is found to be negligible in the coiling fibers tested here. A size effect concerning the ductility in bending and torsion is also found in FDM-extruded PLA filament, which has profound implications for FDM 3D printing. The maximum number of sacrificial bonds which can be all broken in tensile test is three in the small PLA coiling fibers tested here (Figure S6), resulting in an effective toughness 468% − 533% times the performance of the straight fiber benchmark (Table S1). In order to further improve the toughness, material selection is as essential as the structure optimization, just as the damage tolerance property of spider web comes from the integration of structure and the nonlinear material behavior of spider silk [22]. FDM with continuous-fiber reinforced polymer [23, 24] provides new opportunities to develop a good material candidate for microstructured fibers, utilizing ductile polymer matrix and strong continuous-fiber reinforcement. With the understanding of the failure mechanisms of a microstructured fiber in tension, we will be able to further optimize fiber arrays in composites or cellular structures [25] for high energy absorption and damage tolerance properties.

Methods

Instability-assisted fused deposition modeling. A PLA filament (MakerBot PLA Yellow) was extruded through the printing head of a MakerBot 3D printer onto a conveyor belt. The filament was was fused at 230 °C in the heater block, then extruded out of the nozzle. Two nozzles with different diameters (0.3 mm and 1 mm) were used in this paper. An open source 3D printing software ReplicatorG was used to control the speed of the stepper motor. In order to achieve stable deposition, the stepper motor was set at 2 rpm (revolutions per minute) and 8 rpm for the small and large nozzle, respectively. This led to the volume flow rate of 2.53 mm³/s and 10.5 mm³/s, respectively. Due to die swell, the extruded polymer threads had diameters of 0.37 mm and 1.20 mm, respectively. Geometrically similar

coiling fibers were fabricated at $V_E / V_B = 3.71$ and $H / d = 11$. The straight fibers were fabricated at $V_E / V_B = 1$ and $H / d = 11$.

Uniaxial tensile test. Uniaxial tensile test of the coiling fiber was performed on an electromechanical machine (MTS Insight 50 kN) in ambient environment. The fiber was clamped with a constant force of 100N at both ends by a pair of pneumatic grips (TestResources G94) with an air pressure of 100 psi. The crosshead speed was 500 mm/min. Forces were measured with 5 N and 100 N load cell for the small and large fiber respectively. Coiling fibers with 1 to 8 loops were tested, with 10 repetitions each for both small and large fibers.

Three-point bending test. Custom-made acrylic fixtures were used for the three-point bending test of straight fiber on the MTS Insight machine. The diameters of the loading noses and supports are 0.8 mm and 2 mm for the small and large fiber respectively. The spans are 3 mm and 10 mm, respectively. The small and large straight fibers were cut into 5 mm and 16 mm long pieces. Reaction forces of the loading nose were measured with 5 N and 100 N load cell, respectively. The crosshead speed is 84.8 mm/min for the small fiber and 275 mm/min for the large fiber.

Finite element analysis. The geometrical data of the coiling fiber was generated in MATLAB via digital image analysis and then imported into ANSYS to create the mesh. Nonlinear FEA was adopted to simulate the bond breaking and loop unfolding process of the coiling fiber under tension, with both elastic and plastic material model. In the elastic FEA, the fiber is assumed isotropic with Young's modulus $E = 3$ GPa, and Possion's ratio $v = 0.36$. In the plastic FEA, multilinear isotropic hardening plasticity and von Mises yield criterion were used to create the constitutive law, which was calibrated based on the uniaxial tensile test of straight PLA fiber (Figure S2). The elastic FEA modeled the fiber with 3D beam element (BEAM189), while the plastic FEA utilized a beam-solid assembly (Figure S1a). Solid elements (SOLID186) were used in the middle of the coiling loop in order to avoid the convergence difficulty caused by beam elements under large inelastic deformation due to torsional loading [26]. The fiber segment modeled by solid elements shared the same diameter as the one modeled by beam elements. They were connected by rigid surface constraint [27]. In both elastic and plastic FEA, the sacrificial bond was modeled by a 3D beam-to-beam contact [27] with the multipoint constraint (MPC) approach which constrained three translational degrees of freedom of crossing beam elements. The simulation was conducted in a displacement-controlled manner. A force threshold criterion [3] was used to break sacrificial bonds. The displacement was incrementally applied at the pulling end using a do-loop in ANSYS Parametric Design Language (APDL). The reaction force at the pulling end was examined in each step. Once the reaction force reached the threshold, the MPC contact elements were deactivated by the program, simulating the breaking of the sacrificial bond. After the death of the MPC contact elements, the incremental displacement continued to be applied on the model and the simulation restarted based on the solution from the previous run. The breaking sequence and force thresholds of sacrificial bonds were set exactly as in the test.

Acknowledgements

References

1. F. Vollrath and D. P. Knight, *Nature*, 2001, **410**, 541.
2. A. Nova, S. Keten, N. M. Pugno, A. Redaelli and M. J. Buehler, *Nano Letters*, 2010, **10**, 2626-2634.
3. G. E. Fantner, E. Oroudjev, G. Schitter, L. S. Golde, P. Thurner, M. M. Finch, P. Turner, T. Gutsmann, D. E. Morse, H. Hansma and P. K. Hansma, *Biophysical Journal*, 2006, **90**, 1411-1418.
4. G. E. Fantner, T. Hassenkam, J. H. Kindt, J. C. Weaver, H. Birkedal, L. Pechenik, J. A. Cutroni, G. A. G. Cidade, G. D. Stucky, D. E. Morse and P. K. Hansma, *Nature Materials*, 2005, **4**, 612.
5. B. L. Smith, T. E. Schaffer, M. Viani, J. B. Thompson, N. A. Frederick, J. Kindt, A. Belcher, G. D. Stucky, D. E. Morse and P. K. Hansma, *Nature*, 1999, **399**, 761-763.
6. M. J. Harrington, H. S. Gupta, P. Fratzl and J. H. Waite, *Journal of Structural Biology*, 2009, **167**, 47-54.
7. N. M. Pugno, *PLOS ONE*, 2014, **9**, e93079.
8. M. F. Pantano, A. Berardo and N. M. Pugno, *Scientific Reports*, 2016, **6**, 18222.
9. F. Bosia, E. Lepore, N. T. Alvarez, P. Miller, V. Shanov and N. M. Pugno, *Carbon*, 2016, **102**, 116-125.
10. R. Passieux, L. Guthrie, S. H. Rad, M. Lévesque, D. Therriault and F. P. Gosselin, *Advanced Materials*, 2015, **27**, 3676-3680.
11. S. R. Koebley, F. Vollrath and H. C. Schniepp, *Materials Horizons*, 2017, **4**, 377-382.
12. M. K. Jawed, F. Da, J. Joo, E. Grinspun and P. M. Reis, *Proceedings of the National Academy of Sciences*, 2014, **111**, 14663-14668.
13. S. Chiu-Webster and J. R. Lister, *Journal of Fluid Mechanics*, 2006, **569**, 89-111.
14. P. T. Brun, C. Inamura, D. Lizardo, G. Franchin, M. Stern, P. Houk and N. Oxman, *Philosophical Transactions of the Royal Society A: Mathematical, Physical and Engineering Sciences*, 2017, **375**.
15. M. D. Hayes, D. B. Edwards and A. R. Shah, in *Fractography in Failure Analysis of Polymers*, William Andrew Publishing, Oxford, 2015, DOI: https://doi.org/10.1016/B978-0-323-24272-1.00004-0, pp. 48-92.
16. D. Hull, in *Fractography: observing, measuring and interpreting fracture surface topography*, Cambridge University Press, United Kingdom, 1999, pp. 121-150.
17. X. Chen, S. Zhang, D. A. Dikin, W. Ding, R. S. Ruoff, L. Pan and Y. Nakayama, *Nano Letters*, 2003, **3**, 1299-1304.
18. S. Nohut and G. A. Schneider, *Journal of the European Ceramic Society*, 2009, **29**, 1013-1019.
19. G. Eggeler, E. Hornbogen, A. Yawny, A. Heckmann and M. Wagner, *Materials Science and Engineering: A*, 2004, **378**, 24-33.
20. N. A. Fleck, G. M. Muller, M. F. Ashby and J. W. Hutchinson, *Acta Metallurgica et Materialia*, 1994, **42**, 475-487.
21. A. C. M. Chong and D. C. C. Lam, *Journal of Materials Research*, 2011, **14**, 4103-4110.
22. S. W. Cranford, A. Tarakanova, N. M. Pugno and M. J. Buehler, *Nature*, 2012, **482**, 72.
23. R. Matsuzaki, M. Ueda, M. Namiki, T.-K. Jeong, H. Asahara, K. Horiguchi, T. Nakamura, A. Todoroki and Y. Hirano, *Scientific Reports*, 2016, **6**, 23058.
24. M. Domm, J. Schlimbach and P. Mitschang, presented in part at the 21st International Conference on Composite Materials, Xi'an, China, 2017.
25. J. I. Lipton and H. Lipson, *Scientific Reports*, 2016, **6**, 29996.
26. *ANSYS Mechanical APDL Element Reference (Release 15.0)*, ANSYS Inc., Canonsburg, PA, 2013.
27. *ANSYS Mechanical APDL Contact Technology Guide (Release 15.0)*, ANSYS Inc., Canonsburg, PA, 2013.
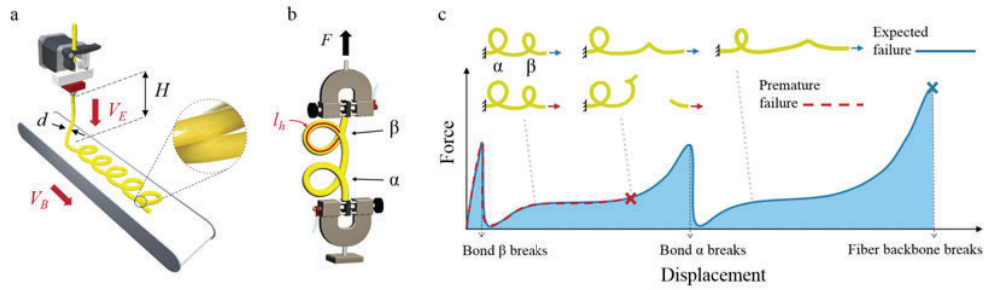
Figure 1. a) Schematic of the IFDM. The ratio of the filament extruding speed V_E to the belt moving speed V_B dictates the fiber pattern on the belt. The ratio of the deposition height H to the fiber diameter d dictates the size of the loop. Sacrificial bonds are formed via fusion at the intersections in the coiling pattern after the polymer is solidified by cooling. b) The produced coiling fiber has a constant hidden length l_h which can be released by the breaking of sacrificial bonds (α, β) in uniaxial tensile test. c) Schematic comparison of the tensile test sequences and force-displacement curves between expected failure (blue solid line) and premature failure (red dashed line). In expected failure, sacrificial bonds α and β break one by one, resulting in a saw-tooth tensile curve. The ultimate axial tensioning after all hidden lengths are released breaks the fiber backbone, leading to high energy absorption indicated by the blue area under the tensile curve. In premature failure, the fiber backbone is broken during the unfolding process of loop β, before bond α breaks. The truncated tensile curve displays reduced fiber strength and energy absorption.
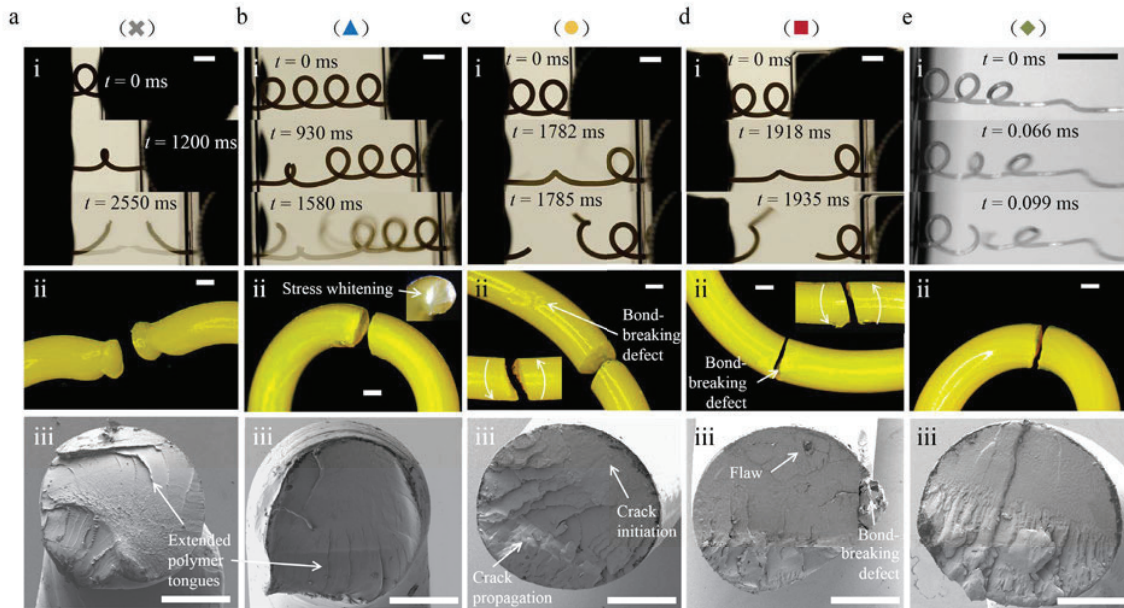

Figure 2. Failure modes observed from uniaxial tensile tests of coiling fibers: axial (✷), bending (▲), torsional (●), bond (■) and dynamic (◆) failure. Each failure mode is characterized by: (i) sequential camera captures of the unfolding process after the breaking of sacrificial bond. Time zero is defined at the breaking of sacrificial bond; (ii) microscopy images of the fracture pieces; (iii) SEM images of the fracture surfaces. All specimens shown here are from the large fiber with a diameter of 1.20 mm, except the camera captures of dynamic failure, which are from the small fiber with a diameter of 0.37 mm for

the sake of convenience in shooting with high speed camera. Scale bars are 5 mm in (i), and 0.5 mm in (ii), (iii).
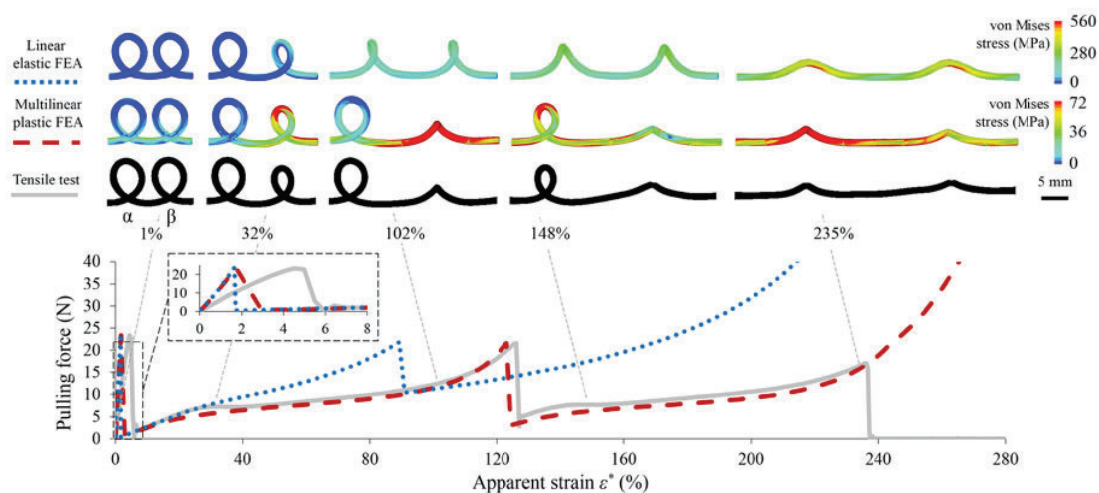

Figure 3. The breaking of sacrificial bonds in two coiling loops under uniaxial tension from linear elastic FEA (blue dotted line), multilinear plastic FEA (red dashed line) and tensile test (grey solid line). The breaking sequence of sacrificial bonds in the FEAs is set the same as that in the tensile test: first bond β, then bond α. The force threshold for each sacrificial bond in the FEAs is also set the same as that in the tensile test: 23.4 N for bond β and 21.6 N for bond α. The unfolding shapes are obtained at five given apparent strain values. The color gradient represents the magnitude of von Mises stress in the FEA contour plots. The FEAs and test results here are all for the large fiber with a diameter of 1.20 mm.
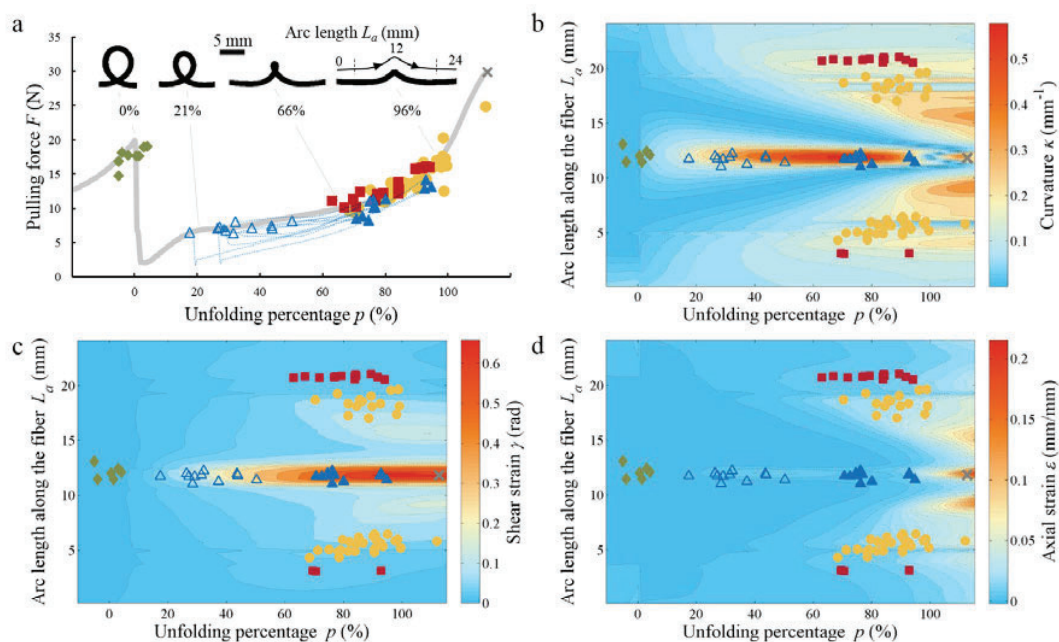

Figure 4. a) Distribution of the five failure modes in coiling fibers illustrated by failure points overlaid on a representative force-displacement curve of a single coiling loop. Failure points are defined as the final break of fiber backbone from the following failure modes: axial (✗), bending (▲), torsional (●),

bond (■) and dynamic (◆) failure. For bending failure, crack initiation (△) and the following force curves (blue dashed lines) are also marked. Local b) curvature, c) shear strain, d) axial strain calculated from the multilinear plastic FEA are used to explain the fracture location of each failure mode along the fiber during the unfolding process. Arc length L_a is calculated based on the loop α in the simulation, starting from the fixed end. The bond-breaking defects locates at $L_a = 3.12$ and 20.31 mm. All failure points here are for the large fiber with a diameter of 1.20 mm.
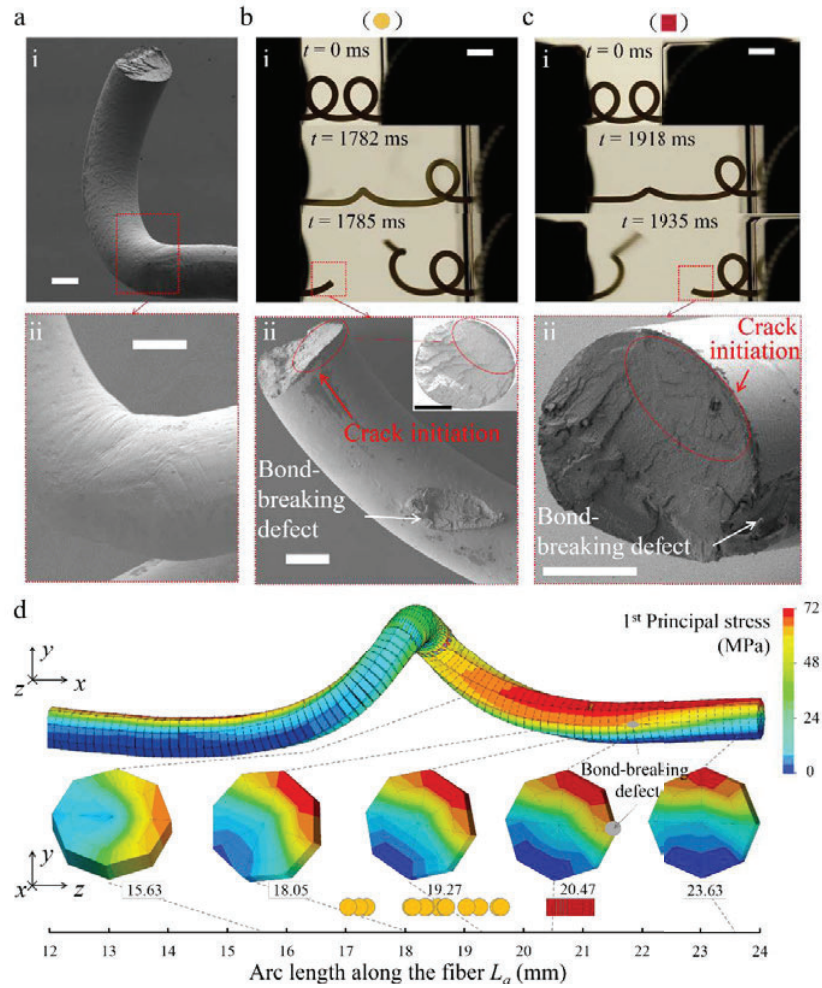
Figure 5. Illustration of the crack initiation in torsional and bond failure due to high local tensile stress: a) SEM images of torsional failure specimen showing large material distortion in the middle of the loop. Fractures of b) torsional failure and c) bond failure specimen are characterized by sequential camera captures and SEM images. The relative location of crack initiation region with reference to the bond-breaking defect in both failure modes can be seen in the SEM images. d) Contour plot of one coiling loop at $p = 80$ % from the plastic FEA. The color gradient represents the magnitude of the first principal stress. Cross-sectional contour plots of the fiber are shown at $L_a = 15.63$, 18.05, 19.27, 20.47 and 23.63 mm along the loop. The inner side of the beam element at $L_a = 20.47$ mm corresponds to the bond-breaking defect. The fracture location along the fiber (at $L_a = 12$ mm to 24 mm) are shown by ● for torsional failure and ■ for bond failure. Both torsional and bond failures can be attributed to a large region of tensile stress. Scale bars are 5 mm in camera captures and 0.5 mm in SEM images.
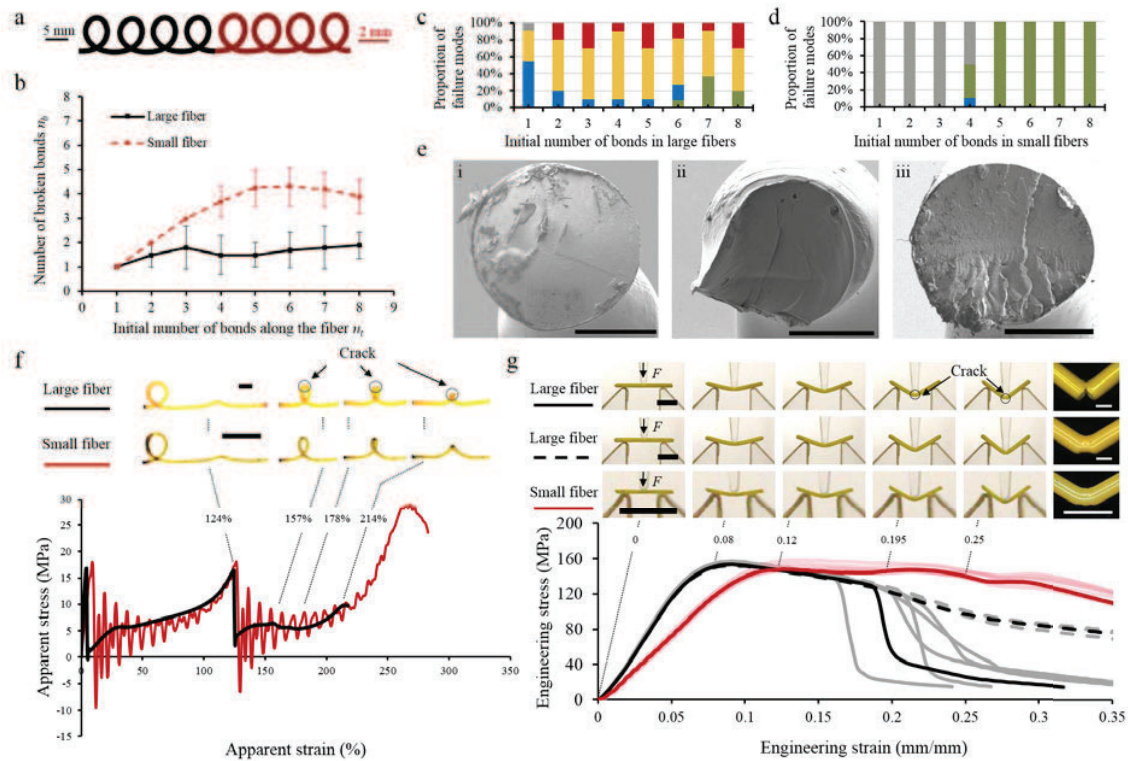
Figure 6. Comparison of the failure behavior in a) two geometrically similar coiling fibers with different diameters: 1.20 mm (in black) and 0.37 mm (in red). b) The number of actually broken bonds n_b in both large and small fibers varying with different initial number of bonds n_t in the uniaxial tensile tests. The error bar stands for the standard deviation based on a sample size of 10 for each data point. The proportion of axial (grey), bending (blue), torsional (yellow), bond (red) and dynamic (green) failures in c) large and d) small fibers varying with different n_t. e) SEM images of the fracture surfaces in axial (i), bending (ii) and dynamic (iii) failures of the small fibers. Scale bars are 0.2 mm. f) Comparison of the unfolding geometries and apparent stress-strain curves of the large (black lines) and small (red lines) fibers with two coiling loops. The oscillations on the red curves are due to the vibration of the 5 N load cell induced by the bond breakage. Scale bars are 5 mm. g) Comparison of the engineering stress-strain curves, test sequences and post-test microscopy images of the large (black lines) and small (red lines) straight fibers in the three-point bending test. At the bottom of the fiber where the bending stress is maximum in tension, the large fiber specimens either show sharp crack or large plastic deformation (corresponding to the black solid and dashed lines respectively on the stress-strain diagram), while all the small fiber specimens show large plastic deformation. All stress-strain curves from ten specimens for each fiber are shown in the plot. Besides the three representative curves, other curves are shown in gray or pink for the large and small fibers respectively to show the measurement deviations. Scale bars are 5 mm in camera captures, and 1 mm in microscopy images.

Supplementary Information

Local strain calculation

The plastic FEA utilized a beam-solid element assembly (Figure S1a). Solid elements were used in the middle of the coiling loop in order to avoid the convergence difficulty caused by beam elements under large inelastic deformation due to torsional loading [1]. Since the solid element does not provide direct cross-sectional outputs for curvature, torsional strain and axial strain along the fiber like the beam element does, we extract nodes displacements from each load substep in the simulation and calculate local strains along the fiber during the unfolding process. Results at the unfolding percentage of 80% are shown here as an example. For the curvature, the trace of center nodes (Figure S1a) in solid elements is rebuilt in MATLAB. A circle is fitted to every three adjacent points along the trace [2]. The apparent curvature κ_a is calculated as the inverse of the radius of the circle. The bending curvature κ (Figure S1b, red markers) which correlates with the bending stress is calculated as $\kappa = \kappa_a - \kappa_i$, where κ_i is the corresponding initial curvature of the fiber center line. The as-calculated κ is equivalent to $\sqrt{\kappa_Y^2 + \kappa_Z^2}$ (Figure S1b, blue markers), where κ_Y and κ_Z are element outputs for the bending curvature about the Y and Z centroid axis of the beam element. The shear strain γ is calculated based on the corner angle of the surface mesh (Figure S1a): $\gamma = \theta_d - \theta_i$, where θ_d is the angle on the deformed mesh, and θ_i is the angle on the initial mesh. The shear strain at each L_a is averaged by 40 values around the circumference (Figure S1c). The as-calculated γ is equivalent to $r\gamma_{TE}$ (Figure S1c, blue markers), where, r is the fiber radius, γ_{TE} is the element output of torsional strain from the beam element. The axial strain is calculated as $\varepsilon = (l_d - l_i)/l_i$, where l_d is the length between two adjacent center nodes after deformation, l_i is the initial length. The as-calculated ε is equivalent to the beam element output of axial strain. Discontinuities exist in all three local strain results at the transition from beam element to solid element. This is caused by the rigid surface constraint which is necessary to assemble beam and solid element.
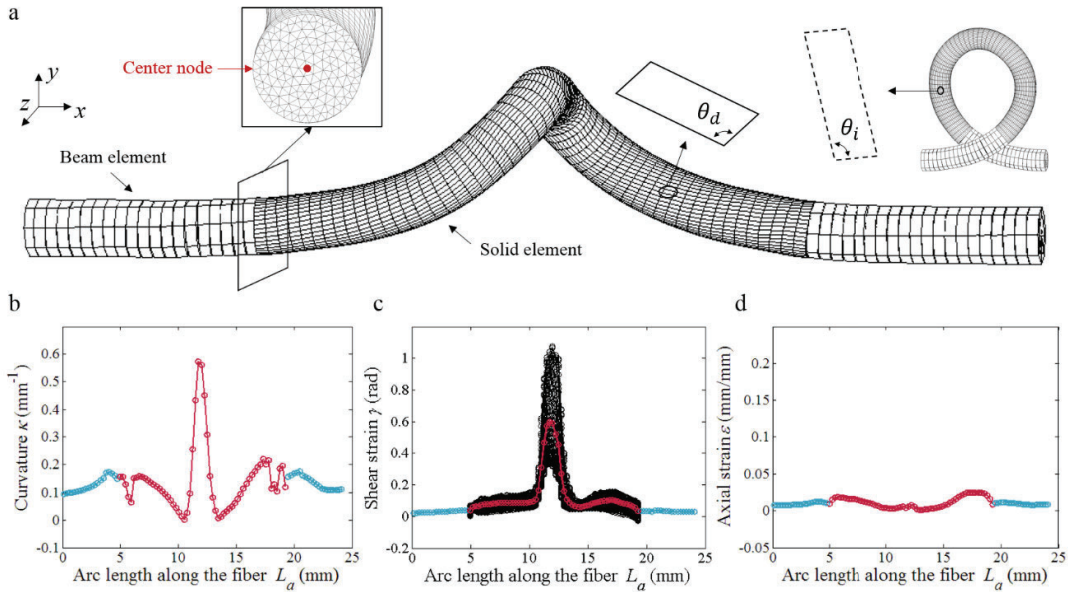

Figure S1. Local strain results calculated from beam and solid elements at the unfolding percentage of 80%: a) deformed meshes of beam and solid elements; b) curvature, c) shear strain, and d) axial strain calculated from beam (blue markers) and solid (red markers) elements. The shear strains in solid elements are averaged over 40 values (black markers) around the circumference at each L_a.
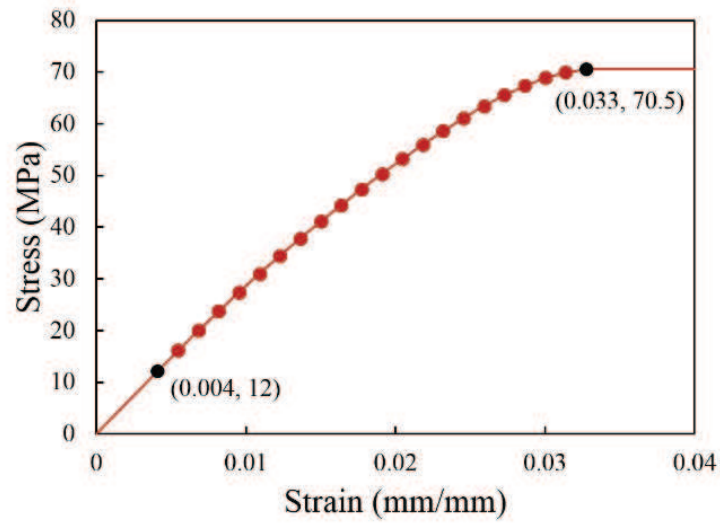
Multilinear plastic FEA

Figure S2 Piece-wise linear stress-strain curve for multilinear isotropic hardening in the plastic FEA. The first stress-strain point defines the yield stress (12 MPa). Subsequent points define the multilinear isotropic hardening behavior of the material. The last point corresponds to the fracture of the fiber in tensile test, while in the plastic FEA, the fiber behaves perfectly plastically after the material reaches the tensile strength (70.5 MPa). The data points are collected from one of the uniaxial tensile tests of straight PLA fiber with the diameter of 1.20 mm (gauge length = 250 mm, strain rate = 0.01 mm/mm/s). The tensile strength with a standard deviation for 7 specimens is 71.3 ± 0.95 MPa.
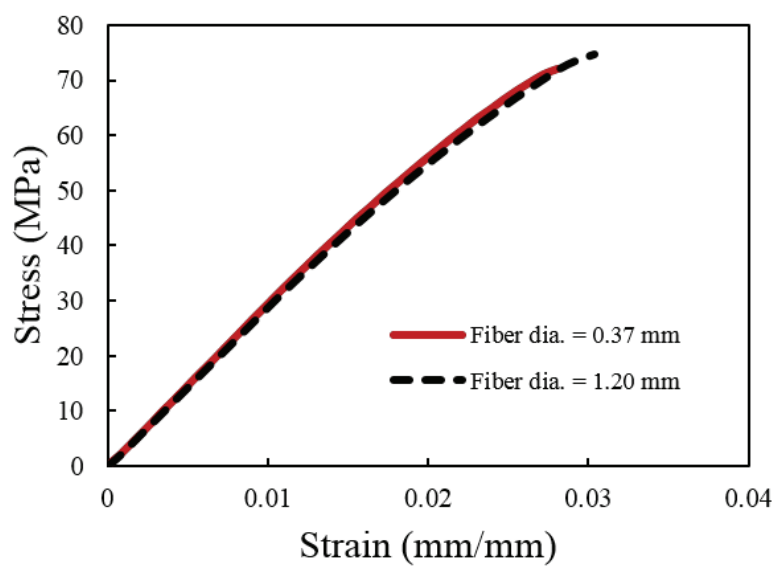
Tensile curves of straight fibers

Figure S3 Stress-strain curves of straight fibers under uniaxial tension. Gauge length is 100 mm and crosshead rate is 500 mm/min for both fibers.

Strain rate estimation

Von Mises strain ε_{VM} (Figure S4a, blue solid line) at the top surface in the middle of the unfolding loop is extracted from the plastic FEA. In order to have the von Mises strain rate $\dot{\varepsilon}_{VM}$ (Figure S4a, red dashed line), we first calculate the equivalent elapsed time t after the breaking of sacrificial bond in the simulation, based on the pulling end displacement in the simulation and actual crosshead speed (8.33 mm/s with an initial acceleration of 52 mm/s^2) in the uniaxial tensile test. Then the local strain rate $\dot{\varepsilon}_{VM}$ is obtained by differentiating ε_{VM} over the elapsed time t. The strain rate reaches the peak of 0.33 mm/mm/s at $p = 35\%$, around which the bending crack initiates at the top middle of the loop (Figure 4a). This peak strain rate is used for both the large and small fibers in the three-point bending test. We approximate the strain rate in dynamic failure by the same method. In order to calculate the instantaneous speed after the breaking of sacrificial bond in dynamic failure, we track the adjacent bond in the traction direction from the high speed camera captures (Figure S4b) and calculate the average pulling speed of the unfolding loop between each frame. The acceleration (1.327×10^5 m/s^2) was obtained by a linear fit (Figure S4c), based on which, we calculate the equivalent elapsed time t_d after the breaking of sacrificial bond in the simulation. The von Mises strain rate (Figure S4d, orange dashed line) in dynamic failure is obtained by differentiating the von Mises strain (Figure S4d, blue solid line) over the elapsed time t_d. The fiber backbone breaks in the middle of the loop within 99 µs after the breaking of sacrificial bond (Figure S4b). The strain rate at the top middle of the loop is 274 mm/mm/s (Figure S4d) at $t_d = 99$ µs. With the acceleration unchanged, the strain rate at the top middle of the loop would reach the peak of 1492 mm/mm/s at $t_d = 235$ µs if the fiber backbone did not break.
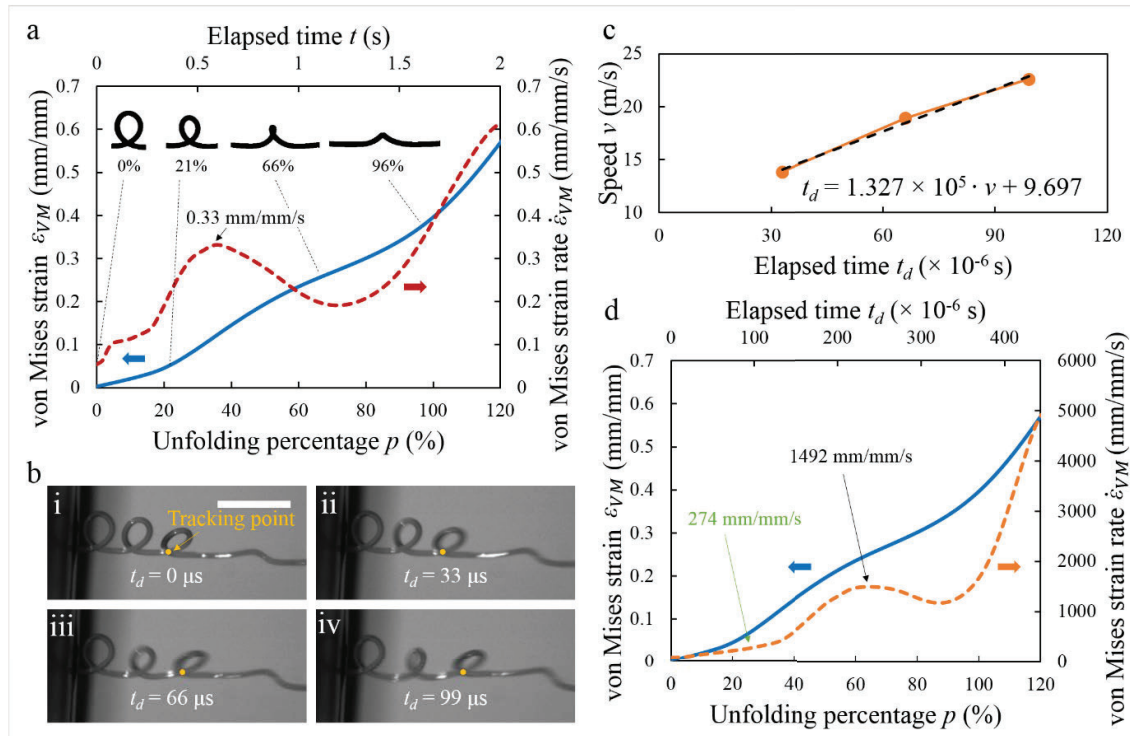

Figure S4. Estimation of the local strain rate at the top surface in the middle of the unfolding loop: a) von Mises strain (blue solid line, left Y axis) and von Mises strain rate (red dashed line, right Y axis) at the top surface in the middle of the unfolding loop, during the normal unfolding process of the loop without dynamic failure. The bottom and top X axis represent the unfolding percentage and elapsed time, respectively. They correspond to each other and serve as different references for the unfolding process.

b) High speed imaging of the loop retraction after the breaking of sacrificial bond in dynamic failure. The speed of the loop retraction at t_d = 33 µs, 66 µs and 99 µs is calculated by measuring the moving distance of the tracking point in ii – iv relative to its initial position at t_d = 0 µs in i. Scale bar is 5 mm. c) Linear fit of the loop retraction speed over elapsed time. d) von Mises strain (blue solid line, left Y axis) and von Mises strain rate (orange dashed line, right Y axis) at the top surface in the middle of the unfolding loop, during the rapid unfolding process of the loop in dynamic failure. Simulation results, such as the von Mises strain and strain rate, are extracted from 101 load substeps and plotted as continuous lines here for the sake of visual demonstration.
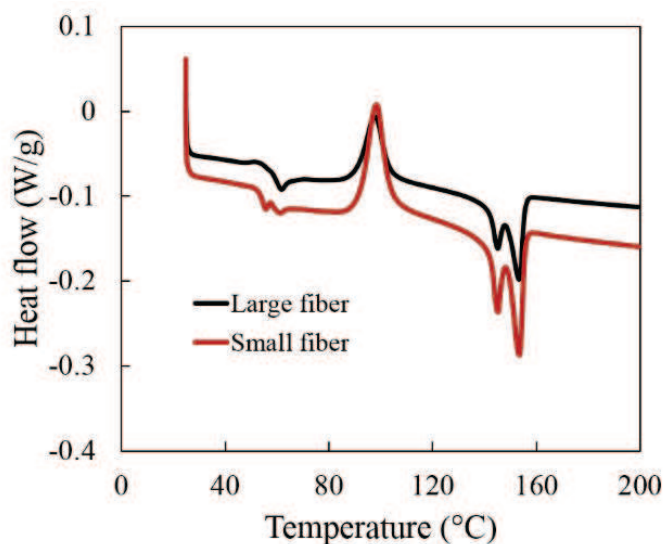
DSC test of large and small fibers

Figure S5. DSC results of FDM-extruded PLA fibers. The fibers were extruded at 230 °C on the conveyor belt in ambient air with two nozzles with different diameters (1 mm and 0.3 mm). The belt speed is equal to the extruding speed. The large and small fibers are 1.2 mm and 0.37 mm in diameter, respectively.

Thermal analysis of PLA fibers was performed in a DSC instrument (DSC Q2000) with the heating program found in the literature [3]. The temperature was first held at 25 °C for 3 min, and then increased to 200 °C with a rate of 2 °C/ min. The samples were cut from the same batch of straight fibers for the three-point bending test. The sample weight was 5.8 mg for the large fiber and 5.2 mg for the small fiber. The degree of crystallinity X_C of the specimen was calculated by the following equation:

$$X_C = \frac{\Delta H_m - \Delta H_c}{\Delta H_{100}} \times 100$$

where, ΔH_m is the enthalpy of fusion, ΔH_c is the enthalpy of cold crystallization, ΔH_{100} is fusion enthalpy of 100% crystalline PLA, which is 93 J/g [3].

The calculated crystallinity is approximately 2.5% for the large fiber and 1.1% for the small fiber, which are around the crystallinity of as-received PLA filament (2.4%) reported in the literature [3].
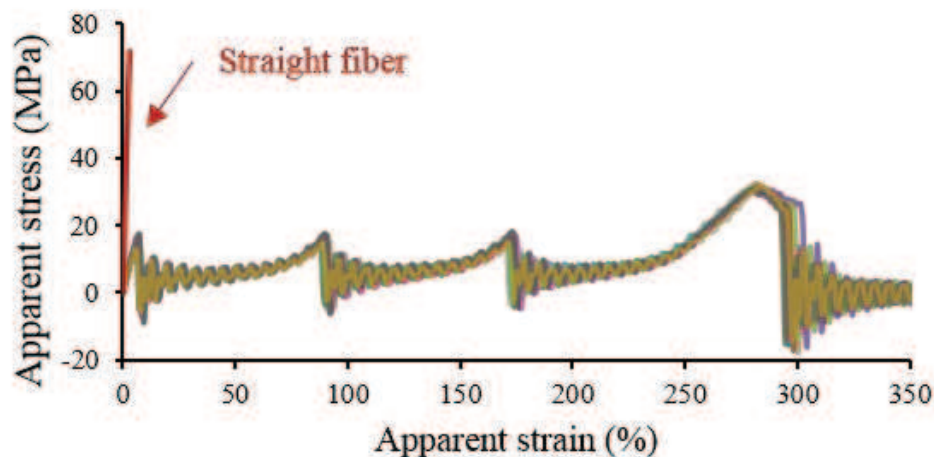
Toughness enhancement

Figure S6 Apparent stress-strain curves of small fiber with three coiling loops. All ten test specimens are plotted to show the deviation. The stress-strain curve of the straight small fiber is also plotted as a benchmark to show the toughness enhancement in coiling fibers.

Table S1 Toughness values of the small fiber with three coiling loops. The benchmark toughness value of the straight fiber is 1.1 kJ/kg.

	Toughness (kJ/kg)		
	Average	Maximum	Minimum
3 coiling loops (small fiber)	5.51	5.86	5.15
%Benchmark	500%	533%	468%

References

1.   *ANSYS Mechanical APDL Element Reference (Release 15.0)*, ANSYS Inc., Canonsburg, PA, 2013.
2.   J. Korsawe, *Circlefit3d - fit circle to three points in 3d space*, MATLAB Central File Exchange. Retrieved March 10, 2017.
3.   M. Ivey, G. W. Melenka, J. P. Carey and C. Ayranci, *Advanced Manufacturing: Polymer & Composites Science*, 2017, **3**, 81-91.